Early warning of the Indian Ocean Dipole using climate network analysis

Zhenghui Lu[a,1], Wenjie Dong[b,c,d,2], Bo Lu[e,2], Naiming Yuan[b,c,d,1,2], Zhuguo Ma[a], Mikhail I. Bogachev[f], and Juergen Kurths[g,h]

aCAS Key Laboratory of Regional Climate Environment for Temperate East Asia, Institute of Atmospheric Physics, Chinese Academy of Sciences, Beijing 100029, China; bSchool of Atmospheric Sciences, Sun Yat-sen University, Zhuhai 519082, China; cKey Laboratory of Tropical Atmosphere-Ocean System, Ministry of Education, Zhuhai 519082, China; dInnovation Group of Earth System Model, Southern Marine Science and Engineering Guangdong Laboratory (Zhuhai), Zhuhai 519082, China; eKey Laboratory for Climate Studies, National Climate Center, China Meteorological Administration, Beijing 100081, China; fDepartment of Radio Engineering Systems, Saint Petersburg Electrotechnical University, Saint Petersburg 197022, Russia; gDepartment of Physics, Humboldt University, Berlin 12489, Germany; and hDepartment of Complexity Science, Potsdam Institute for Climate Impact Research, Potsdam 14473, Germany

In recent years, the Indian Ocean Dipole (IOD) has received much attention in light of its substantial impacts on both the climate system and humanity. Due to its complexity, however, a reliable prediction of the IOD is still a great challenge. In this study, climate network analysis was employed to investigate whether there are early warning signals prior to the start of IOD events. An enhanced seesaw tendency in sea surface temperature (SST) among a large number of grid points between the dipole regions in the tropical Indian Ocean was revealed in boreal winter, which can be used to forewarn the potential occurrence of the IOD in the coming year. We combined this insight with the indicator of the December equatorial zonal wind in the tropical Indian Ocean to propose a network-based predictor that clearly outperforms the current dynamic models. Of the 15 IOD events over the past 37 y (1984 to 2020), 11 events were correctly predicted from December of the previous year, i.e., a hit rate of higher than 70%, and the false alarm rate was around 35%. This network-based approach suggests a perspective for better understanding and predicting the IOD.

Indian Ocean Dipole | climate network | prediction

The Indian Ocean Dipole (IOD) is a zonal dipole mode of the sea surface temperature (SST) that occurs interannually in the tropical Indian Ocean (TIO) (1, 2). A positive (negative) IOD features a below (above) normal SST off the Sumatran coast and a warming (cooling) over the western equatorial Indian Ocean. Ever since the severe floods in East Africa in 1997, which were induced by an extreme positive IOD (pIOD) event (2), the IOD has attracted much attention. Many studies showed that the IOD can affect the climate not only in the Indian Ocean rim countries but also in other more distant regions (3–5). In the past decades, great efforts have been made to reveal the mechanisms of the IOD, but the IOD prediction is still challenging, which further limits the associated seasonal climate predictions.

One reason for the difficulties in predicting the IOD is that the TIO is complex, with multiple processes interacting. Previous studies reported that there are different triggers that may initiate the occurrence of the IOD, such as the El Niño–Southern Oscillation (ENSO) (6, 7), the Indonesian Throughflow (8), intraseasonal disturbances (9), the subtropical IOD (10), springtime Indonesian rainfall (11), and the interhemispheric pressure gradient over the maritime continent (12). In addition, the development of the IOD in boreal summer was found to be controlled by different feedback processes in the Indian Ocean, including the thermocline–SST, cloud–radiation–SST, and evaporation–SST–wind feedbacks (1, 9, 13). As a typical atmosphere–ocean coupled mode, the IOD is thus a complex phenomenon that is sensitive to changes in multiple associated processes. The dilemma is that it is not clear which of the above-mentioned triggers play the main role in a given IOD event. For instance, ENSO events have

been well recognized as a major external force to trigger IOD events via altering the Walker Circulation (4), but there are still many cases (e.g., 1996, 2012, and 2019) where an IOD event is not accompanied by an ENSO event, and the different IOD classifications (3, 14, 15) make the ENSO–IOD interactions even more complicated. The formation of the IOD was found to be associated with both the forcing outside the Indian Ocean and internal variability within the basin (16), but there is no certain physical mechanism that combines all the associated forcings and feedback processes. Moreover, as a phenomenon with quasi-biennial frequency (1, 17), two (or three) pIOD events may occur in consecutive years (18), and sometimes there may even be a few consecutive years with no remarkable IOD events. These complex characteristics increase the difficulty of the IOD prediction (19–23). In general, skillful predictions of the IOD events by climate models can only be made one season ahead (22, 23) and occasionally two or three seasons for strong events (9, 18). A rapid drop of the IOD predictive capability across the boreal winter has been well recognized as the winter predictability barrier

Significance

The Indian Ocean Dipole (IOD), an air–sea coupled phenomenon over the tropical Indian Ocean, has substantial impacts on the climate, ecosystems, and society. Due to the winter predictability barrier, however, a reliable prediction of the IOD has been limited to 3 or 4 mo in advance. Our work approaches this problem from a new data-driven perspective: the climate network analysis. Using this network-based method, an efficient early warning signal for the IOD event was revealed in boreal winter. Our approach can correctly predict the IOD events one calendar year in advance (from December of the previous year) with a hit rate of higher than 70%, which strongly outperforms current dynamic models.

(24), suggesting a lack of precursor signals due to the low signal-to-noise ratio. To better cope with the IOD-associated impacts, continuous efforts are thus required to improve the predictive capability for IOD events.

In this study, we investigated this issue. Previous studies revealed different trigger and development mechanisms that contribute to the formation of the IOD. However, it is unclear whether there are any TIO states favorable for IOD onset, given the fact that the previously proposed triggering mechanisms do not work in all cases. It was recognized that a shallower thermocline depth in the eastern Indian Ocean is a precondition that favors the pIOD activity on decadal time scales (25, 26). Are there any preconditions on interannual or even biennial scales that may lead to an improved early warning of the IOD onset? To address these questions, we employed a recently proposed approach, the climate network analysis (27), to examine possible relationships among the grid points in the dipole regions. The climate network, as the name implies, is a network of the climate system with grid points (or stations) considered as nodes and the relations (i.e., correlations) between each pair of nodes as links (27–29). By studying climate systems in terms of climate networks, one may obtain more detailed information, including the topological structure (30, 31) and the dynamic evolutions (32, 33). A particular advantage of the climate network approach is that by taking into account all the interior grid points in the climate system, even weak signals (that could appear seemingly negligible when considered alone) contribute substantially to the overall system dynamics, eventually leading to significant effects when exhibiting cooperative behavior (34). Based on this advantage, the climate network analysis has been successfully applied

in the forecasting of Atlantic Meridional Overturning Circulation (35, 36); the predicting of extreme precipitation events (37); and in particular, an early forecast of the onset of the Indian Summer Monsoon (38). By analyzing the cooperative behaviors among the interior nodes in the tropical Pacific and north Pacific, early warning signals have been detected for the onset of El Niño events (39, 40) and the phase change of the Pacific Decadal Oscillation (PDO) (34). In this study, we employed this approach to investigate IOD events, especially the interactions of the SSTs between the dipole regions, to see whether there are early signals arising from the cooperative behaviors among the grid points, or in other words, to detect possible TIO states that favor the development of the IOD.

Results

Detecting the Early Warning Signal. In this work, daily and monthly SST anomalies within the spatial domain from 40°E to 110°E and 10°N to 10°S were analyzed (Fig. 1A). Based on the monthly data from 1982 to 2020, the empirical orthogonal function (EOF) analysis was first applied to determine the border of the dipole regions (Fig. 1A or *SI Appendix*, Fig. S1), according to which 190 nodes were included in the western part of the dipole (the blue grid points in Fig. 1A) and 156 nodes in the eastern part (the red grid points in Fig. 1A) for further analysis. Based on the daily SST anomaly (SSTA) data, connections between these two regions were calculated using climate network approaches to identify the links between each node in the western region and each node in the eastern region. In this study, the link between each pair of nodes is defined as the similarity of the SSTA, where the link strength is quantified using a correlation-based technique
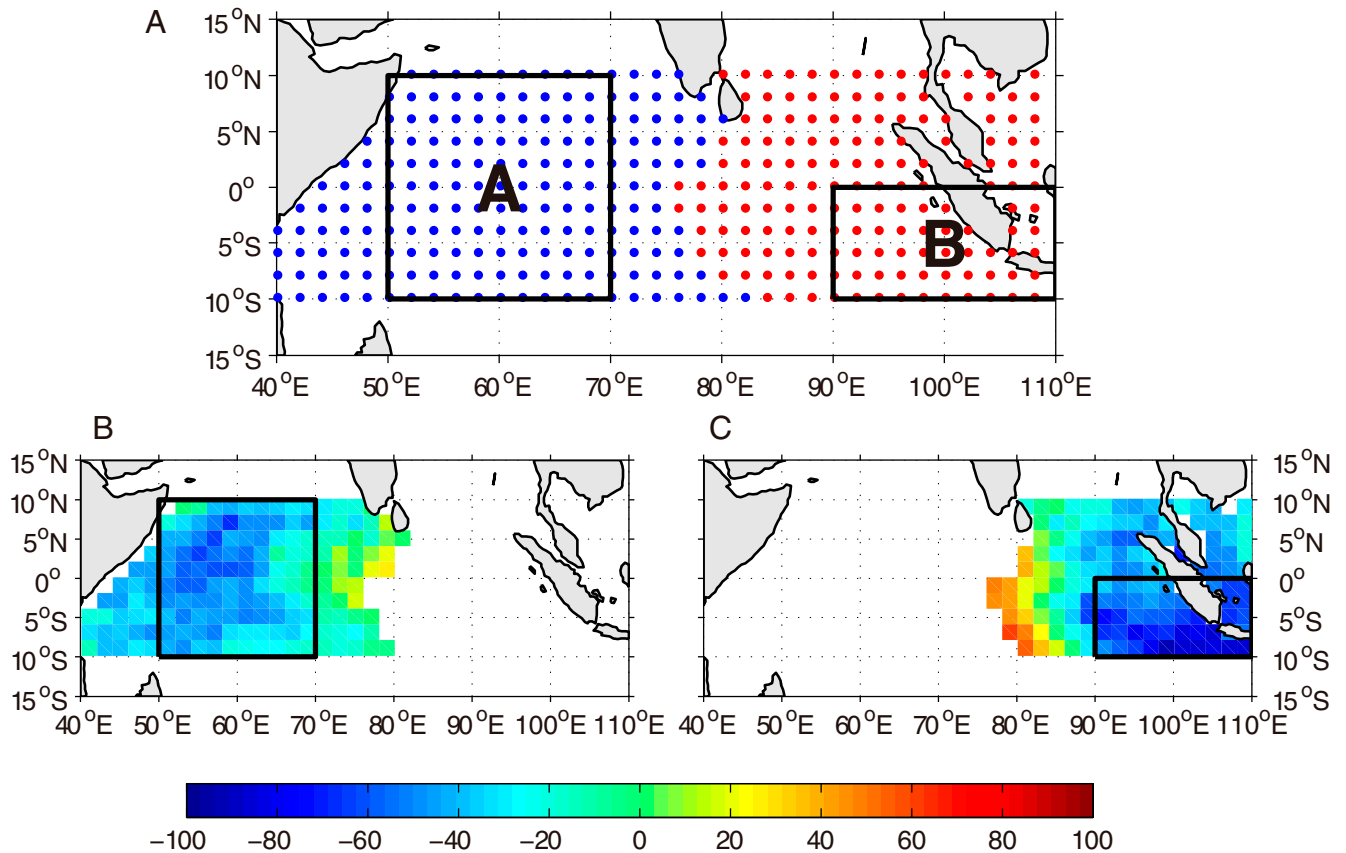
Fig. 1. The constructed climate network in the TIO and its composite of node degree. (A) The regions are determined according to the definition of the IOD based on EOF2 of SSTA. The eastern and western regions are represented by blue and red nodes, respectively. (B) The spatial distribution of composite of node degree in the eastern region. (C) Same as B but in the western region. Regions A (black box from 50°E to 70°E and 10°S to 10°N) and B (black box from 90°E to 110°E and 10°S to the equator) are part of the eastern and western regions, respectively, used to calculate DMI.

(*Materials and Methods*). The contribution of a given node (e.g., node i in the western region) in the network is thus estimated by adding up the link strengths between this node and all the nodes in the other region (e.g., the eastern region), with the total link strength characterizing the node degree. In Fig. 1 *B* and *C*, the node degree for each node in the studied regions is shown. Clear negative patterns are found in the regions where the well-known dipole mode index (DMI) is defined. The black boxes (50°E to 70°E, 10°S-10°N, region A; 90°E to 110°E, 10°S to the equator, region B) denote the regions where the regional average SSTAs are used to calculate the DMI (*Materials and Methods*). Since on average, the negative node degree indicates the opposite changing directions of the SSTAs in both regions, the results from our climate network analysis reflect the basic feature of the zonal dipole mode in the TIO.

To study the temporal evolution of the climate network and its relation with the IOD events, we used the DMI index to define the IOD events. If the mean DMI is above (below) 0.5 °C (−0.5 °C) for three consecutive months, a pIOD (negative IOD [nIOD]) event is detected (Fig. 2 and *SI Appendix*, Table S1). The node degree is determined in a moving time window of 1 y (using all days of the year, i.e., 365 d), and the total degree (TD) is obtained as the sum of all the node degrees in region A (or B) (*Materials and Methods*). As suggested in refs. 39, 40, the TD measures the interactions between the dipole regions. Accordingly, a negative TD that is larger in its absolute value indicates a stronger negative connection between both regions (Fig. 2*A*). As expected, they are negative most of the time, reflecting the characteristics of the dipole pattern. There is a quasi-annual cycle in the TD time series indicated by the spectral density analysis (*SI Appendix*, Fig. S2), and the peak usually ap-

pears in December (Fig. 2). By repeating the calculations of the TD using randomly selected nodes around the world (*Materials and Methods*), a threshold (red curve in Fig. 2*A*) is estimated to determine whether the observed negative TD is above the significance level of 95%. Taking each year as a unit, the years exceeding the threshold are detected (green triangles in Fig. 2*A*), indicating that there the anticonnections between the dipole regions are statistically significant. Compared to the DMI index (Fig. 2*B*), a fascinating finding is that the years with statistically significant negative TD values are frequently followed by years with IOD events. Of the total 15 IOD events from 1984 to 2020, 11 IOD events (6 pIODs and 5 nIODs) occurred in the next year after a significant TD appeared, suggesting that the TD may serve as a potential early warning signal for the onset (regardless of the sign) of IOD events.

The question is, however, where does this early warning signal originate from? Recall the definition of the TD. Its magnitude depends on the link strength between each pair of nodes from the dipole regions and the number of negative links. Fig. 2*C* shows that the latter is the main reason for the enhancement of the TD. In other words, the statistically significant negative TD is mainly induced by the fact that more grid points between the dipole regions are negatively linked (see *SI Appendix*, Fig. S3, for the detailed locations with enhanced cooperativity). This cooperative behavior among a large number of grid points can amplify signals from noises, which is a typical advantage of the climate network analysis in detecting precursors. A more detailed study further revealed that the statistically significant negative TD may have originated from the quasi-biennial variations of the TIO. As shown in *SI Appendix*, Figs. S4 and S5, after filtering out the quasi-biennial variability from the SSTA in TIO, by
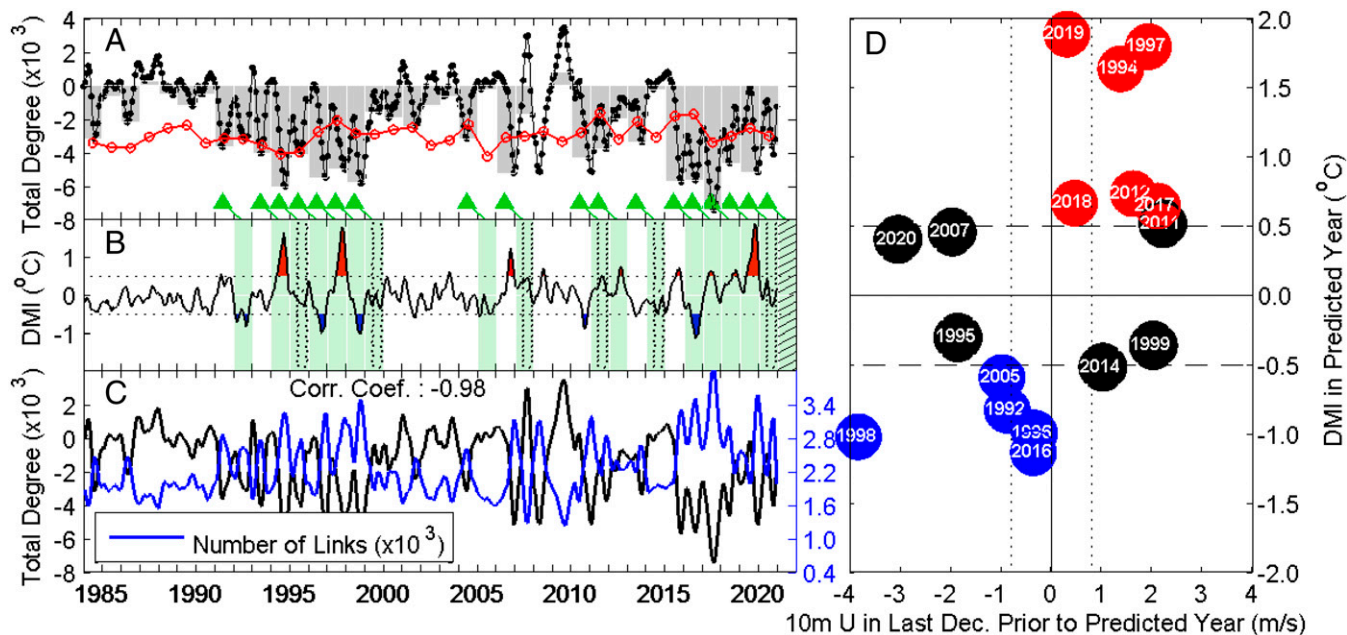
Fig. 2. Early warning signal based on climate network and 10-m zonal wind indicator. (*A*) The TD $TD(t)$ shows the fluctuation of early warning signals for IOD (black dotted line). The gray bars show $TD(y)$ derived from $TD(t)$ in each year, and the red dotted line shows the threshold $TD^{TH}(y)$ for $TD(y)$ with significance at the confidence level of 0.05. The green triangles represent the years when $TD(y)$ exceeds $TD^{TH}(y)$, indicating the early warning signals are released 1 y in advance. (*B*) The green bars show the next years followed by early warning signals. The black curve is the 3-mo running mean DMI, and the pIOD and nIOD events are represented by red and blue areas above and below 0.5 °C and −0.5 °C (dotted lines), respectively, for consecutive 3 mo. The green bars with nothing, dots, and oblique lines represent correct alerts, false alerts, and an alert that needs to be confirmed in the future, respectively. (*C*) The relationship between the TD (the black line, which is the same as in *A*) and the number of negative links connecting regions A and B (the blue line) is highly negative correlated with a correlation coefficient of −0.98. (*D*) The diagram of 10-m zonal wind index (*Materials and Methods*) in December of years when early warning signals are released and the IOD amplitude in the next year. The blue and red circles represent nIOD and pIOD events, respectively, among the correct alerts, and the black ones represent the false alerts. The numbers in the circles stand for the year when early warning signals are released. The vertical dotted lines indicate ±0.5 SD of December wind anomalies. The horizontal dashed lines represent 0.5 °C and −0.5 °C for DMI index.

Lu et al.
Early warning of the Indian Ocean Dipole using climate network analysis

PNAS | 3 of 9
https://doi.org/10.1073/pnas.2109089119

repeating the climate network analysis, the early warning signal was no longer detectable. Previous studies have reported that the IOD has variabilities of multiple time scales (41). While the background state of the eastern Indian Ocean thermocline depth may modulate the frequency of the IOD on decadal scales (25, 26), the quasi-biennial variability in the TIO theoretically can contribute to the early warning of the IOD. The dilemma, however, is that one cannot simply use the quasi-biennial variability to predict the IOD due to its multiscale characteristics. As shown in *SI Appendix*, Fig. S6, more than half of the IOD events are incorrectly forecasted if using the IOD state of the previous year as a judgement for the occurrence of the IOD in the following year. Therefore, taking the advantages of the climate network analysis, the significant negative TD arising from the cooperative behaviors of a large number of gird points may serve as an objective detection of the TIO state that favors seesaw-like change. Although this TIO state does not necessarily induce an IOD event, as the arising of IOD events also depends on how the trigger and feedback processes work, the significant negative TD may still be considered as a reasonable precondition of the IOD in the following year.

Determining the Signs of the Forewarned IOD Event. Using the climate network approach, we detected a signal that forewarns the occurrence of IOD events by the end of the previous year. However, the detected early warning signal can only inform us whether an IOD event may occur in the following year, without any information about the sign. Since the early warning signal is associated with the quasi-biennial variations of the TIO (*SI Appendix*, Figs. S4 and S5), a straightforward way to determine the sign of the forewarned IOD event is to use the equatorial zonal wind over the Indian Ocean (*SI Appendix*, Fig. S7), which has been well recognized to have a quasi-biennial cycle and is closely coupled with the IOD (1).

In the remainder of this section, we analyze the 10-m zonal wind field over the TIO. A crucial finding is that the composite wind fields in December are characterized by the opposite spatial patterns, typically preceding different (positive or negative) IOD events occurring in the following year (*SI Appendix*, Fig. S8). This result is confirmed with more details in Fig. 3, which shows a clear temporal evolution of the air–sea coupled system in the Indian Ocean. Unlike the SST–wind coupling, where the easterly (westerly) equatorial zonal wind prevails in the boreal summer and autumn and coevolves with positive (negative) IOD events, in the previous December, the wind seems to be still statistically related to the signs of the IOD events, but the direction is opposite. From December to the next October, the continuous evolution of the wind field and the corresponding changes of the depth of the 20 °C isotherm can be clearly observed (Fig. 3). In addition to the composite analysis, the temporal evolution of individual events was also studied (e.g., the pIOD event in 1994 and the nIOD event in 1998; *SI Appendix*, Figs. S9 and S10),
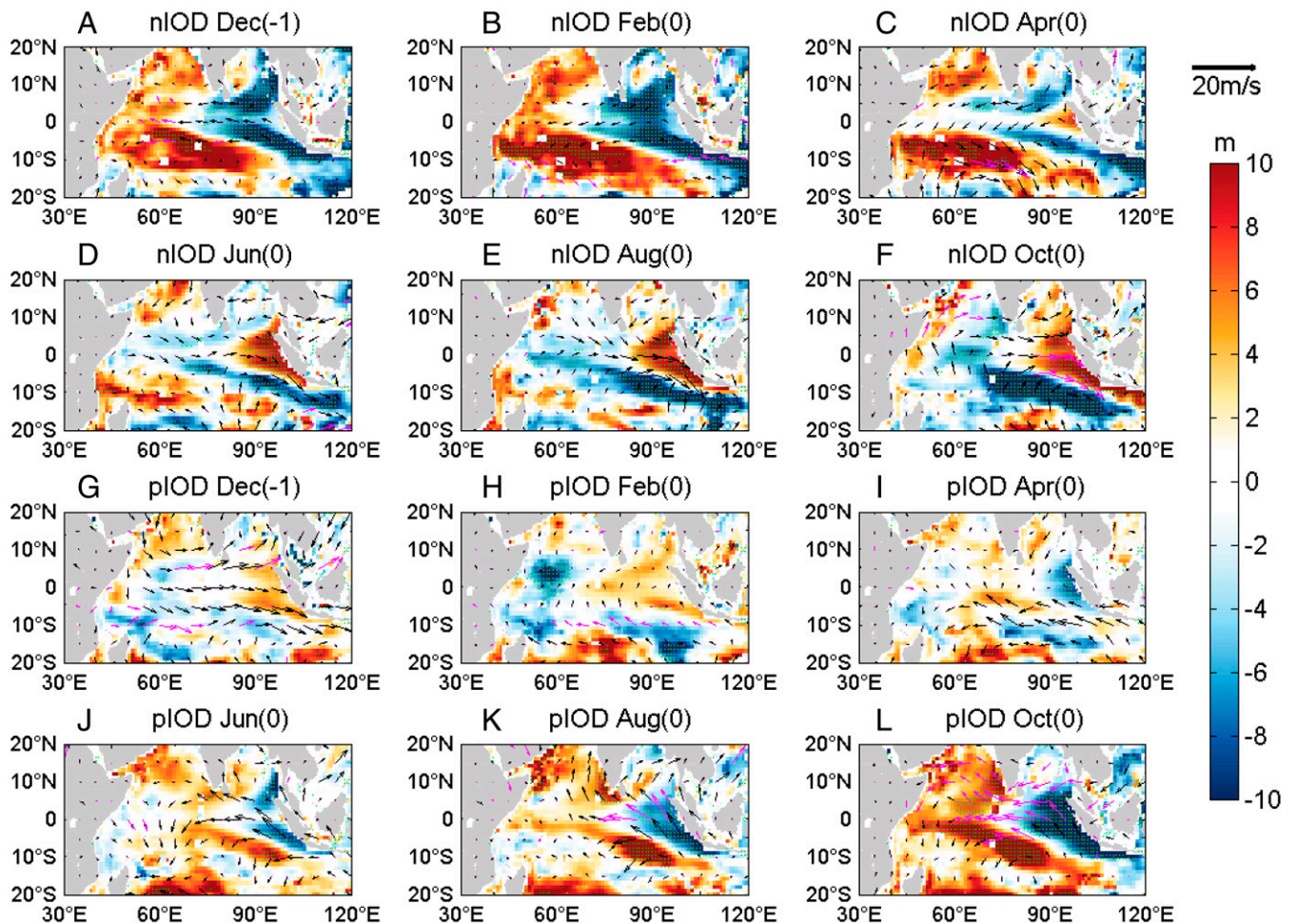
Fig. 3. Composite analysis of 10-m wind and the depth of 20 °C isotherm for pIOD and nIOD. (*A–F*) The composite of 10-m wind (arrows) and the depth of 20 °C isotherm (colors) for the nIOD of correct alerts from the previous December in which the forecast starts initially to the current October in which IOD reaches its peak. (*G–L*) The same as *A–F* but for pIOD. The nodes with magenta arrows and green dots are significant at the confidence level of 0.05 for 10-m wind and the depth of 20 °C isotherm, respectively.

which further highlighted the potential relations between the December zonal wind direction and the signs of the IOD event in the following year. Based on this phenomenon, we define the new index U_{eD} as the December mean zonal wind over the region from 70°E to 100°E and 5°S to 5°N (*SI Appendix*, Fig. S8C). By referring to the directions of U_{eD}, we found that the correctly forewarned IOD events by the climate network analysis (Fig. 2B) are clearly divided into two groups. As shown in Fig. 2D, among the 17 early warnings alerted by the TD, there are 11 alerts that correctly predicted the occurrence of IOD events (red and blue circles). After taking U_{eD} into account, all the pIOD and nIOD events are successfully separated. Therefore, U_{eD} can serve as a useful indicator to predict the signs of the predicted IOD events.

It is worth noting that the equatorial zonal wind in December received little attention in previous studies. This is because December is at the time when the signal-to-noise ratio is low and the prediction of the IOD is difficult. The indicative effect of U_{eD} may come from the quasi-biennial cycle of the system, where the equatorial zonal wind direction in December is usually opposite to that in the following boreal summer and autumn. This biennial tendency could be related to the monsoon–ocean feedback (13), the tropospheric biennial oscillation (42), and the quasi-biennial component of ENSO (13) and its combination mode (6), but more detailed studies are still needed to better understand this phenomenon. Here the use of the equatorial zonal wind direction is only a possible (but not perfect) way to judge the phase of the forewarned IOD event. A more physically reasonable judgment of the sign could be made by analyzing the subsequent trigger and feedback processes, but this will lead to a shorter warning time. In addition, we also would like to emphasize that the early warning skills of this study mainly come from the climate network

analysis. Using only the quasi-biennial variability of the system cannot give a trustworthy prediction of the IOD. As shown in *SI Appendix*, Fig. S6, if the onset of the IOD as well as its phase are predicted according to the IOD state from the previous year, only 5 out of the 15 events are correctly forecasted, while the false alarm rate is as high as 66.7%.

Evaluation of the Early Warning Skill. Based on the above results, we suggest a network-based approach for the early warning of IOD events. It consists of two main steps. First, check whether the total number of degrees between the dipole regions A and B is significantly enhanced within the considered year. If yes, an IOD event is predicted in the next boreal summer and autumn. Second, the direction of the equatorial zonal wind in December (i.e., U_{eD}) could be further used to determine the sign of the predicted IOD event. If a westerly (easterly) equatorial wind prevails in December, a pIOD (nIOD) event is expected. Following this strategy, one can predict the occurrence of IOD events from the previous December. As shown in Fig. 4A, among the 15 IOD events during the study period from 1984 to 2020 (see also *SI Appendix*, Table S1), 11 events are correctly predicted; i.e., we obtained a hit rate of 73.3% (black open circle in Fig. 4B). Particularly, the consecutive years without IOD events (i.e., 2000 to 2004) and the years with consecutive pIOD events (i.e., 2017 to 2019) are correctly predicted, indicating a promising early warning skill. Besides the hit rate, the false alarm rate was also estimated as the ratio of the false alarms to all the alarms issued by the approach. Of the 17 alarms sounded by the network-based approach, there are 6 false alarms, i.e., a rate of 35.3%. For more details, we further checked the results for different IOD events separately. For the pIOD, six (out of nine) events
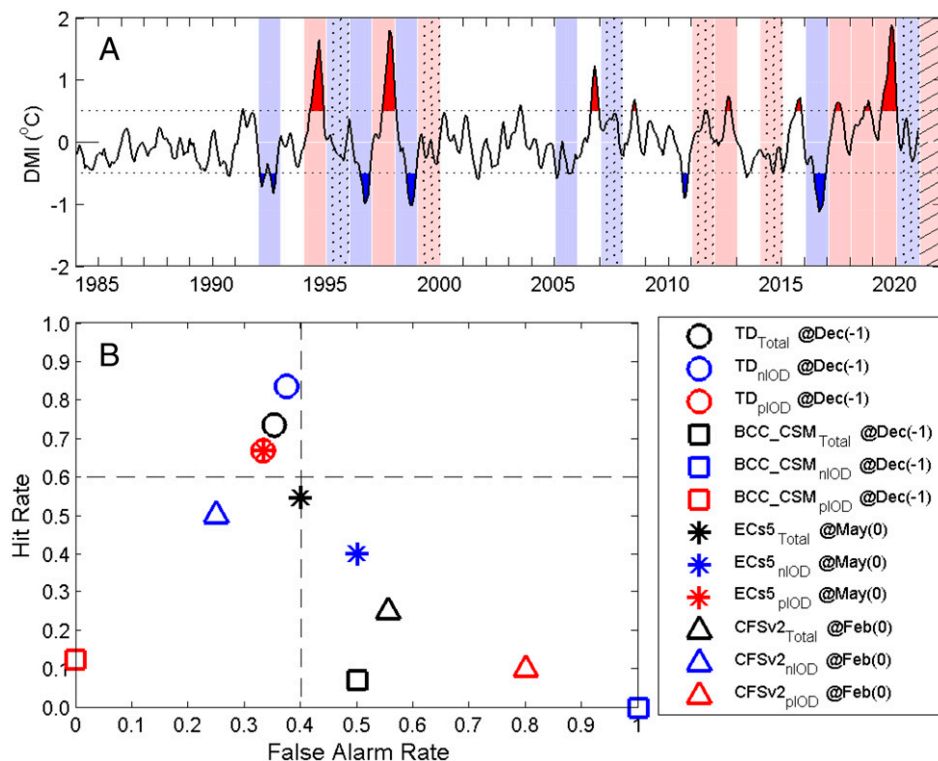
Fig. 4. Results of the network-based approach and the dynamical models. (A) Result of the network-based approach on IOD events forecast. The forecasted pIOD and nIOD events are represented by red and blue bars, respectively, and the real IOD events are represented by the red and blue areas based on its definition. The black curve is the 3-mo running mean DMI, and the dotted lines stand for 0.5 °C and −0.5 °C. The meanings of red or blue bars with dots and oblique lines are the same as in Fig. 2B. (B) The diagram of false alarm rate and hit rate (*Materials and Methods*) on the performance of the network-based approach and dynamical models. The circles, squares, asterisks, and triangles stand for performance of the network-based approach, the BCC_CSM, the ECs5, and the CFSv2, which forecast initially in the previous December, the previous December, the current May, and the current February, respectively. The black, blue, and red colors of the four marks represent the performance of these four approaches on the total, nIOD, and pIOD events.

Lu et al.
Early warning of the Indian Ocean Dipole using climate network analysis

PNAS | 5 of 9
https://doi.org/10.1073/pnas.2109089119

are correctly predicted, i.e., a hit rate of 66.7% and a false alarm rate of 33.3% (red open circle in Fig. 4*B*). For the nIOD, the hit rate is even higher (83.3%), and the false alarm rate is 37.5% (blue open circle in Fig. 4*B*). Of the six nIOD events that occurred from 1984 to 2020, the network-based approach successfully predicted five events. By combining the hit rate with the false alarm rate, we further calculate the Heidke skill score (HSS) (*Materials and Methods*) (37) to better assess the early warning skills. For the network-based approach, the HSS is 0.4510 (*SI Appendix*, Table S2).

Next, we compare the performance of this approach with the commonly used climate models. Three operational climate prediction models were considered in this study, including the Beijing Climate Center Climate System Model (BCC_CSM), the European Centre for Medium-Range Weather Forecasts (ECMWF) seasonal forecast system version 5 (ECs5), and the National Centers for Environmental Prediction (NCEP) coupled forecast system model version 2 (CFSv2). As shown in *SI Appendix*, Fig. S11, the BCC_CSM provides long-term consecutive forecasts throughout each year, which allows for an evaluation of the forecasting skill starting from the previous December, the same as in our approach. The ECs5 and the CFSv2 forecast six and nine consecutive months and are initialized every month. To capture the IOD peak phase from September to November, the evaluations of the ECs5 and the CFSv2 started from May and February, respectively. The results of the three models are shown in Fig. 4*B* as open squares, asterisks, and open triangles. Compared to our network-based approach, the hit rates of the dynamic models are much lower, and the false alarm rates are higher. The BCC_CSM has the same forecast starting month (i.e., December) as the network-based approach, but the hit rate is only around 10% (black open square in Fig. 4*B*), which is much lower than that of the network-based approach (73.3%). In fact, there are only 2 y that are predicted to have IOD events in the BCC_CSM. As shown in *SI Appendix*, Fig. S11 and Table S1, one is a correct forecast of a pIOD in 2018, and the other one is an incorrect forecast of an nIOD in 2015. By taking both the hit rate and false alarm rate into account, the HSS value is equal to 0 for the BCC_CSM (*SI Appendix*, Table S2). The low forecast skills indicate the winter predictability barrier (19), which seems to have limited effect on the network-based approach. By delaying the forecast starting time, the performance of the dynamic models is enhanced. As the open triangles show, when it is initialized in February, the CFSv2 has a hit rate of 26.7% (black triangle in Fig. 4*B*), and half of the nIOD events were correctly forecasted (blue triangle). However, the false alarm rate is still high (55.6%). Compared to the network-based approach that starts the forecast 2 mo earlier, the overall forecasting skill of the CFSv2 is still much lower with HSS = 0.0303. Forecasting from May, the ECs5 has shown the best performance among the three models (asterisks in Fig. 4*B*). The hit rate successfully exceeds 50%, and the false alarm rate is 40%. The forecast skill for the pIOD events (red asterisks) was found to be comparable with the network-based approach. However, it is worth noting that the overall skill is still lower with HSS = 0.2394, and most importantly, the forecast starts at the time when the IOD events are about to develop clearly, which is already 5 mo later than the network-based approach. Accordingly, although there is still room for improvement in the network-based approach (i.e., the false alarm rate is a bit high), compared with the current models, it provides a clear superiority in predicting the IOD events. To test the robustness, different IOD classifications (3, 14, 15) were used (*SI Appendix*, Table S3), and their corresponding HSS values were obtained (*SI Appendix*, Table S4). Regardless of the time span (*SI Appendix*, Table S3), most IOD events identified by different classifications are consistent with each other. As a result, the predictive skill based on the HSS values (*SI Appendix*, Table S4) was basically unchanged, indicating that

this network-based approach is the best, while ECs5 is better than BCC_CSM and CFSv2.

Discussion

Over a long period of time, the prediction of the IOD dynamics has been limited by the winter predictability barrier, and overcoming this barrier remains a crucial challenge. In this work, we approach this problem from a data-driven perspective: the climate network analysis. The key advantage of this approach is that it takes into account all the interior grid points in the climate system, such that even weak signals that are otherwise often neglected contribute to the overall network connectivity, eventually leading to significant effects when exhibiting cooperative behavior. Based on this advantage, we reveal that a significant strengthening of the negative connections in the IOD dipole regions during the boreal winter is associated with the occurrence of the IOD in the following year. In this way, 11 IOD events (out of the 15 events during the years from 1984 to 2020) were correctly forewarned. By referring to the equatorial zonal wind directions in December, the signs of IOD events can be further determined. Using this network-based approach, more than 70% of the IOD events during the past 37 y were successfully forewarned from the December of the previous year. This skill strongly outperforms that of the current dynamic models, even for the dynamic models that start the forecast a few months later.

An interesting facet of the results is that the early warning signal seems to have multidecadal variability. It arises more frequently in the 1990s and 2010s (Fig. 2*A*), which relates very well with the fact that more IOD events occurred in these two separate decades. In the past years, the decadal variability of the IOD has been widely and deeply studied (41, 43, 44), and the background state of the eastern Indian Ocean thermocline depth is suggested as an important factor (25, 26). Affected by the decadal variations from the Pacific via both oceanic teleconnections (i.e., through the Indonesian Throughflow) and atmospheric teleconnections (i.e., wind forcings), the eastern Indian Ocean thermocline exhibits decadal variations that can further modulate the frequency of the IOD on decadal scales (25, 26, 45–47). In this study, since the early warning signal is considered a measure of the TIO state that favors the seesaw-like change of the SSTA in the TIO, its multidecadal variability thus indicates that the seesaw-like change of the SSTA is easier to trigger when the eastern Indian Ocean thermocline depth is shallower. Although the detection of the early warning signal is associated with the quasi-biennial variations of the TIO (*SI Appendix*, Figs. S4 and S5), the successful capture of the decadal variability of the IOD reconfirmed the superiority of this network-based approach, which is far beyond the idea of simply using the quasi-biennial variability to predict the IOD (*SI Appendix*, Fig. S6).

We emphasize that the early warning signal detected from the climate network analysis is mainly attributed to the cooperative behaviors of a large number of grid points in the TIO, not the relatively weak spatially averaged link strengths (*SI Appendix*, Fig. S3). This is in line with the well-known fact that the signal-to-noise ratio is low in boreal winter when the previous IOD disappears and a new one is about to be initiated. Accordingly, it is difficult to identify specific processes from boreal winter to link with the onset of the IOD, which is well recognized as the winter predictability barrier (24). Here we touched this issue alternatively by monitoring the SST state of the TIO. When an increasing number of the grid points between the dipole regions are negatively linked, even if the average link strength is weak, we may be able to forewarn a possible IOD onset in the following year. Not only can this typical advantage of climate network analysis be used for the early warning of the IOD, it also has potential in the study of other climatic events, e.g., ENSO (39, 40) or PDO (34). Its outstanding ability in detecting precursors especially when the signal-to-noise ratio is low thus

may attract attentions from a broader audience. Of course, one should note that whether the forewarned event will eventually arise also depends on how the trigger and feedback processes work (e.g., see *SI Appendix*, Fig. S12, where the composites of 10-m wind and the depth of 20 °C isotherm for the incorrect alerts are shown).

Combining with the equatorial zonal wind directions in December allows us to make a judgement on the IOD phase. However, this is not a perfect way that relies much on the biennial tendency of the equatorial zonal wind. For example, from the early warning signal an IOD event in 2021 was forewarned (Fig. 2), and the phase is predicted as positive using data by December 2020 (*SI Appendix*, Fig. S13). However, the biennial tendency of the equatorial zonal wind was disrupted by two consecutive La Niña events in 2020/2021 and 2021/2022, which lead the IOD in 2021 toward negative phase. A similar case is also found in 1999. Accordingly, a further combination of the network-based approach with subsequent climatic processes is needed, and an extension of the approach using additional metrics [i.e., the correlation and phase-analysis-based metrics (48) and causality analysis (49)], or a more generalized approach based on combined network analyses covering both the Indian Ocean and the Pacific Ocean, may be helpful to improve the early warning skills of the approach. Besides, the network-based approach can forewarn the occurrence of IOD events, but it is incapable of predicting the event magnitude. A combination of the climate network approach with an analysis of the system complexity, as indicated by a recent study on the El Niño forecast (50), might be helpful and worthy of further research. These challenges go beyond the focus of this study but deserve special attention in the future.

Materials and Methods

In this work, daily and monthly SSTA of National Oceanic and Atmospheric Administration (NOAA) Optimum Interpolation SST V2 datasets (51, 52) for the time period from 1982 to 2020 with the horizontal resolution of $2° \times 2°$ were analyzed. The research domain covers the TIO from 40°E to 110°E and 10°N to 10°S. There are 346 grid points (nodes) in total. Based on the monthly SSTA, EOF analysis was applied, and the first and the second modes are shown in *SI Appendix*, Fig. S1. The EOF1 describes the Indian Ocean basin-wide warming (IOBW) (53) (explaining 40.1% of the total variation; *SI Appendix*, Fig. S1A), whose time series (PC1) is highly correlated with the mean SSTA over the TIO (*SI Appendix*, Fig. S1B). The EOF2 (explaining 15.8% of the total variation) displays a dipole mode (*SI Appendix*, Fig. S1C) which is identified as the IOD. According to the EOF2 spatial pattern, 190 nodes are classified into the western part of the dipole (blue grids in Fig. 1A) and 156 nodes in the eastern part (red grids in Fig. 1A). The time series of PC2 measures the temporal variations of the IOD, but in this study we used the well-known DMI to describe the IOD event. The DMI is defined as the difference of regional average SSTA between region A (50°E to 70°E, 10°S to 10°N) and region B (90°E to 110°E, 10°S to the equator). From Japan Agency for Marine-Earth Science and Technology (JAMSTEC), we obtained the monthly DMI records, which were calculated based on the NOAA Optimum Interpolation SST V2 dataset (51). A positive (negative) IOD event is defined if the 3 mo running mean DMI is ≥ 0.5 °C (≤ -0.5°C) for consecutive 3 mo. From 1984 to 2020, there are 15 IOD events in total with 9 positive and 6 negative events (*SI Appendix*, Table S1). The time series of PC2 and the DMI are highly correlated (in *SI Appendix*, Fig. S1D). In addition, we also employed the monthly 10-m wind with $1° \times 1°$ horizontal resolution and subsurface temperatures with $1° \times 1°$ horizontal resolution and 41 vertical levels (1 to 2,000 m). Both datasets share the same time period with SSTA. The 10-m wind data were obtained from ECMWF Reanalysis v5 (ERA5) (54), and the subsurface temperature data were obtained from the Institute of Atmospheric Physics (IAP), Chinese Academy of Sciences (CAS) (55). We used the subsurface temperatures to calculate the depth of 20 °C isotherm. Annual cycles in all the above-mentioned records have been removed before analysis.

In order to evaluate the performance of the approach proposed in this work, we also analyzed the DMI forecasts from three dynamical models (*SI Appendix*, Fig. S11): the BCC_CSM, the ECs5, and the CFSv2. For the BCC_CSM, we adopted the hindcast and real-time forecast initialized in every December from 1991 to 2018, which make climate predictions for

12 consecutive months (January to December). For the ECs5, the hindcasts initialized in every May from 1993 to 2016 are analyzed, which give 6-mo predictions (June to November) to capture the mature IOD in boreal fall. As for the CFSv2, 36 forecasts are provided from 1984 to 2019, with nine consecutive months (March to November) forecasted for each year after being initialized in February.

Climate Network. The daily SSTA is used to construct the climate network. To avoid potential influences of the IOBW pattern (i.e., the EOF1), we first removed the TIO average SSTA to obtain $T_k(t)$ for each grid point. In the research domain (Fig. 1A), the grid points are considered as nodes in the climate network. For each pair of nodes between the western and eastern region (blue and red nodes in Fig. 1A), we computed for each 30th day t in the considered time span from January 1984 to December 2020 the cross-correlations with time lags θ between 0 and 200 d, as shown:

$$\begin{cases} C_{i,j}^t(\theta) = \dfrac{\langle T_i(t-\theta)T_j(t)\rangle - \langle T_i(t-\theta)\rangle\langle T_j(t)\rangle}{\sqrt{\langle(T_i(t-\theta)-\langle T_i(t-\theta)\rangle)^2\rangle\langle(T_j(t)-\langle T_j(t)\rangle)^2\rangle}} \\ C_{i,j}^t(-\theta) = \dfrac{\langle T_i(t)T_j(t-\theta)\rangle - \langle T_i(t)\rangle\langle T_j(t-\theta)\rangle}{\sqrt{\langle(T_i(t)-\langle T_i(t)\rangle)^2\rangle\langle(T_j(t-\theta)-\langle T_j(t-\theta)\rangle)^2\rangle}} \end{cases}, \quad [1]$$

where i and j represent the nodes in the western and eastern region, respectively, and the brackets denote an average over the last 365 d (as a time window) before t. For each time point t, the link strength (39, 40) is thus defined using the maximum, the mean, and the SD of the 401 cross-correlation coefficients, as the coefficient W,

$$W_{i,j}(t) = \frac{C_{i,j}^t(\theta^*) - \langle C_{i,j}^t(\theta)\rangle}{\sqrt{\langle(C_{i,j}^t(\theta) - \langle C_{i,j}^t(\theta)\rangle)^2\rangle}}, \quad [2]$$

where θ^* is a specific value of θ at which $C_{i,j}^t(\theta^*)$ is the maximum value among the 401 correlation coefficients. It is worth noting that the link strength can be either positive or negative, depending on the signs of the maximum absolute cross-correlations. For a given node i in the western region, by summing the links connected with all the nodes in the eastern region, the node degree K (27) is determined as

$$K_i(t) = \sum_{j \in EasternRegion} W_{i,j}^t. \quad [3]$$

This equation also applies for the calculation of node degree in the eastern region. The spatial distributions of the node degree in both western and eastern regions are shown in Fig. 1 B and C, where the enhanced areas are highly coincident with the regions A and B, indicating that the node degree indeed reflects the dipole features of the IOD. By summing all the node degrees in region A or B, the TD (30) is defined as

$$TD(t) = \sum_{i \in A, j \in B} W_{i,j}(t), \quad [4]$$

which measures how the two regions are linked with each other. In this work, $TD(t)$ is the metric we used for the early warning of IOD events.

Threshold. To determine whether the calculated $TD(t)$ is physically active, we defined a threshold for each time point t using spatial random test. For each node j in region B, we calculated the link strengths between j and other nodes that are randomly chosen around the globe. By randomly choosing 121 nodes (the same node number as in region A), one could obtain the node degree for node j. After repeating this process 1,000 times for each node in region B at each time point t, we get the threshold value for each node degree at the 95% significant level, defined as $K_j^{TH}(t)$. Accordingly, the threshold for the TD is defined as

$$TD^{TH}(t) = \sum_{j \in B} K_j^{TH}(t). \quad [5]$$

Once the $TD(t)$ calculated from the observational data exceeds the threshold $TD^{TH}(t)$, an early warning signal will be released. It is worth noting that in practice, we take each year as a unit and make the early warning annually. This means that we only compare the maximum absolute $TD(t)$ value in each year (denoted as $TD(y)$) with the maximum $TD^{TH}(t)$ in the same year (denoted as $TD^{TH}(y)$). Normally, the $TD(t)$ displays a downward spike in most years (Fig. 2A). Accordingly, the $TD(y)$ is usually the minimum of the downward spike. However, it should be noted that $TD(y)$ and $TD(y + 1)$ cannot share the same downward spike to avoid the reuse of a potential early warning signal. This means if a $TD(t)$, as a part of the downward spike from the last year y, has a large absolute value at the beginning of the year $y + 1$, we do not consider it anymore as a potential candidate of $TD(y + 1)$. One should also note that the threshold at a given time point is calculated using data from the past 365 d. As a result, there are temporal variations in the threshold.

Lu et al.
Early warning of the Indian Ocean Dipole using climate network analysis

PNAS | 7 of 9
https://doi.org/10.1073/pnas.2109089119

The Network-Based Approach. In order to forewarn the IOD events, the approach proposed in this work consists of two steps: 1) One needs to check whether the calculated TD $TD(y)$ exceeds the threshold $TD^{TH}(y)$ or not. If yes, an IOD event is expected in the coming year. 2) One needs to check the mean equatorial zonal wind over the region from 70°E to 100°E and 5°S to 5°N in December (defined as U_{eD}). A westerly (easterly) U_{eD} indicates a positive (negative) IOD event in the next year. This network-based approach relies on data mining and is able to make an early warning of the IOD from the December of the previous year. For estimating the performance of our approach on the IOD forecast, the hit rate for total (positive/negative) events, which is defined as the percentage of the correctly alerted total (positive/negative) IOD events in the total (positive/negative) IOD events, and the false alarm rate for total (positive/negative) events, which is defined as the ratio of the total (positive/negative) false alarm numbers to the total (positive/negative) alarm numbers, are proposed here (Fig. 4*B*).

HSS. In order to better demonstrate the predictive skill for each prediction approaches mentioned here, we employed the HSS (37) to assess their predictive skill, which considers both the correct and incorrect alarms. It is defined as

$$HSS = \frac{2(ad - bc)}{(a + c)(c + d) + (a + b)(b + d)} \qquad [6]$$

for a skill comparison versus randomness. a and b represent the number of alarms that are correctly and incorrectly sounded, respectively. c denotes the times of IOD events that are missed by the early warning signal TD, while d counts the times when neither an alarm is sounded nor a IOD occurs. HSS = 0 represents a uniformly random warning, while HSS = 1 represents a perfect skill. The values (a, b, c, and d) for computing HSS can be found in *SI Appendix*, Table S2.

Data Availability. The data supporting the findings of this study are publicly available and can be downloaded from the links as follows: NOAA daily and monthly SST (51, 52), https://psl.noaa.gov/data/gridded/data.noaa.oisst.v2.highres.html and https://psl.noaa.gov/data/gridded/data.noaa.oisst.v2.html; ERA5 monthly 10-m wind (54), https://www.ecmwf.int/en/forecasts/datasets/reanalysis-datasets/era5; and IAP monthly subsurface temperature at different depths (55), ftp://www.ocean.iap.ac.cn/cheng/CZ16_v3_IAP_Temperature_gridded_1month_netcdf/. The monthly DMI data were obtained from the JAMSTEC, and one may request the data by contacting JAMSTEC at dmo@jamstec.go.jp. The codes that support the findings of this study are available from GitHub, https://github.com/luzhenghui/IOD_CN_code. MATLAB code (*.m) data have been deposited in GitHub (https://github.com/luzhenghui/IOD_CN_code). All other study data are included in the article and/or *SI Appendix*.

1. N. H. Saji, B. N. Goswami, P. N. Vinayachandran, T. Yamagata, A dipole mode in the tropical Indian Ocean. *Nature* **401**, 360–363 (1999).
2. P. J. Webster, A. M. Moore, J. P. Loschnigg, R. R. Leben, Coupled ocean-atmosphere dynamics in the Indian Ocean during 1997–98. *Nature* **401**, 356–360 (1999).
3. N. Saji, T. Yamagata, Possible impacts of Indian Ocean dipole mode events on global climate. *Clim. Res.* **25**, 151–169 (2003).
4. K. Ashok, Z. Guan, N. Saji, T. Yamagata, Individual and combined influences of ENSO and the Indian Ocean dipole on the Indian summer monsoon. *J. Clim.* **17**, 3141–3155 (2004).
5. Y. Qiu, W. Cai, X. Guo, B. Ng, The asymmetric influence of the positive and negative IOD events on China's rainfall. *Sci. Rep.* **4**, 4943 (2014).
6. M. F. Stuecker *et al.*, Revisiting ENSO/Indian Ocean Dipole phase relationships. *Geophys. Res. Lett.* **44**, 2481–2492 (2017).
7. W. Zhang, Y. Wang, F. F. Jin, M. F. Stuecker, A. G. Turner, Impact of different El Niño types on the El Niño/IOD relationship. *Geophys. Res. Lett.* **42**, 8570–8576 (2015).
8. H. Annamalai *et al.*, Coupled dynamics over the Indian Ocean: Spring initiation of the zonal mode. *Deep Sea Res. II Top. Stud. Oceanogr.* **50**, 2305–2330 (2003).
9. B. Lu *et al.*, An extreme negative Indian Ocean Dipole event in 2016: Dynamics and predictability. *Clim. Dyn.* **51**, 89–100 (2018).
10. J. Feng, D. Hu, L. Yu, How does the Indian Ocean subtropical dipole trigger the tropical Indian Ocean dipole via the Mascarene high? *Acta Oceanol. Sin.* **33**, 64–76 (2014).
11. H. Wang, R. Murtugudde, A. Kumar, Evolution of Indian Ocean dipole and its forcing mechanisms in the absence of ENSO. *Clim. Dyn.* **47**, 2481–2500 (2016).
12. B. Lu, H. L. Ren, What caused the extreme Indian Ocean Dipole event in 2019? *Geophys. Res. Lett.* **47**, e2020GL087768 (2020).
13. T. Li, B. Wang, C. Chang, Y. Zhang, A theory for the Indian Ocean dipole–zonal mode. *J. Atmos. Sci.* **60**, 2119–2135 (2003).
14. G. Meyers, P. McIntosh, L. Pigot, M. Pook, The years of El Niño, La Niña, and interactions with the tropical Indian Ocean. *J. Clim.* **20**, 2872–2880 (2007).
15. A. Pepler, B. Timbal, C. Rakich, A. Coutts-Smith, Indian Ocean Dipole overrides ENSO's influence on cool season rainfall across the eastern seaboard of Australia. *J. Clim.* **27**, 3816–3826 (2014).
16. Y. Yang *et al.*, Seasonality and predictability of the Indian Ocean Dipole mode: ENSO forcing and internal variability. *J. Clim.* **28**, 8021–8036 (2015).
17. K. Ashok, Z. Guan, Y. Toshio, A look at the relationship between the ENSO and the Indian Ocean Dipole. *J. Meteorol. Soc. Jpn. II* **81**, 41–56 (2003).
18. J. J. Luo, S. Behera, Y. Masumoto, H. Sakuma, T. Yamagata, Successful prediction of the consecutive IOD in 2006 and 2007. *Geophys. Res. Lett.* **35**, L14S02 (2008).
19. J. J. Luo, S. Masson, S. Behera, S. Shingu, T. Yamagata, Seasonal climate predictability in a coupled OAGCM using a different approach for ensemble forecasts. *J. Clim.* **18**, 4474–4497 (2005).
20. Q. Song, G. A. Vecchi, A. J. Rosati, Predictability of the Indian Ocean sea surface temperature anomalies in the GFDL coupled model. *Geophys. Res. Lett.* **35**, L02701 (2008).
21. M. Zhao, H. H. Hendon, Representation and prediction of the Indian Ocean dipole in the POAMA seasonal forecast model. *Q. J. R. Meteorol. Soc.* **135**, 337–352 (2009).
22. L. Shi *et al.*, How predictable is the Indian Ocean dipole? *Mon. Weather Rev.* **140**, 3867–3884 (2012).

23. H. Liu, Y. Tang, D. Chen, T. Lian, Predictability of the Indian Ocean Dipole in the coupled models. *Clim. Dyn.* **48**, 2005–2024 (2017).
24. J. J. Luo, S. Masson, S. Behera, T. Yamagata, Experimental forecasts of the Indian Ocean dipole using a coupled OAGCM. *J. Clim.* **20**, 2178–2190 (2007).
25. H. Annamalai, J. Potemra, R. Murtugudde, J. P. McCreary, Effect of preconditioning on the extreme climate events in the tropical Indian Ocean. *J. Clim.* **18**, 3450–3469 (2005).
26. C. C. Ummenhofer, A. Biastoch, C. W. Boning, Multidecadal Indian Ocean variability linked to the Pacific and implications for preconditioning Indian Ocean dipole events. *J. Clim.* **30**, 1739–1751 (2017).
27. A. A. Tsonis, K. L. Swanson, P. J. Roebber, What do networks have to do with climate? *Bull. Am. Meteorol. Soc.* **87**, 585–596 (2006).
28. A. Gozolchiani, S. Havlin, K. Yamasaki, Emergence of El Niño as an autonomous component in the climate network. *Phys. Rev. Lett.* **107**, 148501 (2011).
29. J. F. Donges, Y. Zou, N. Marwan, J. Kurths, The backbone of the climate network. *Europhys. Lett.* **87**, 48007 (2009).
30. A. Radebach, R. V. Donner, J. Runge, J. F. Donges, J. Kurths, Disentangling different types of El Niño episodes by evolving climate network analysis. *Phys. Rev. E Stat. Nonlin. Soft Matter Phys.* **88**, 052807 (2013).
31. J. Fan, J. Meng, Y. Ashkenazy, S. Havlin, H. J. Schellnhuber, Network analysis reveals strongly localized impacts of El Niño. *Proc. Natl. Acad. Sci. U.S.A.* **114**, 7543–7548 (2017).
32. Y. Wang *et al.*, Dominant imprint of Rossby waves in the climate network. *Phys. Rev. Lett.* **111**, 138501 (2013).
33. N. Boers *et al.*, Complex networks reveal global pattern of extreme-rainfall teleconnections. *Nature* **566**, 373–377 (2019).
34. Z. Lu, N. Yuan, Q. Yang, Z. Ma, J. Kurths, Early warning of the pacific decadal oscillation phase transition using complex network analysis. *Geophys. Res. Lett* **48**, e2020GL091674 (2021).
35. M. Van Der Mheen *et al.*, Interaction network based early warning indicators for the Atlantic MOC collapse. *Geophys. Res. Lett.* **40**, 2714–2719 (2013).
36. Q. Y. Feng, J. P. Viebahn, H. A. Dijkstra, Deep ocean early warning signals of an Atlantic MOC collapse. *Geophys. Res. Lett.* **41**, 6009–6015 (2014).
37. N. Boers *et al.*, Prediction of extreme floods in the eastern Central Andes based on a complex networks approach. *Nat. Commun.* **5**, 5199 (2014).
38. V. Stolbova, E. Surovyatkina, B. Bookhagen, J. Kurths, Tipping elements of the Indian monsoon: Prediction of onset and withdrawal. *Geophys. Res. Lett.* **43**, 3982–3990 (2016).
39. J. Ludescher *et al.*, Improved El Nino forecasting by cooperativity detection. *Proc. Natl. Acad. Sci. U.S.A.* **110**, 11742–11745 (2013).
40. J. Ludescher *et al.*, Very early warning of next El Niño. *Proc. Natl. Acad. Sci. U.S.A.* **111**, 2064–2066 (2014).
41. L. Krishnamurthy, V. Krishnamurthy, Decadal and interannual variability of the Indian Ocean SST. *Clim. Dyn.* **46**, 57–70 (2016).
42. G. A. Meehl, J. M. Arblaster, J. Loschnigg, Coupled ocean-atmosphere dynamical processes in the tropical Indian and Pacific Oceans and the TBO. *J. Clim.* **16**, 2138–2158 (2003).
43. K. Ashok, W. L. Chan, T. Motoi, T. Yamagata, Decadal variability of the Indian Ocean dipole. *Geophys. Res. Lett.* **31**, L24207 (2004).
44. L. Zhang, Y. Du, W. Cai, Low-frequency variability and the unusual Indian Ocean dipole events in 2015 and 2016. *Geophys. Res. Lett.* **45**, 1040–1048 (2018).
45. L. L. Trenary, W. Han, Local and remote forcing of decadal sea level and thermocline depth variability in the South Indian Ocean. *J. Geophys. Res.* **118**, 381–398 (2013).
46. Y. Li, W. Han, A. Hu, G. A. Meehl, F. Wang, Multidecadal changes of the upper Indian Ocean heat content during 1965–2016. *J. Clim.* **31**, 7863–7884 (2018).

8 of 9 | PNAS
https://doi.org/10.1073/pnas.2109089119

Lu et al.
Early warning of the Indian Ocean Dipole using climate network analysis

47. Y. Li, W. Han, F. Wang, L. Zhang, J. Duan, Vertical structure of the upper-Indian Ocean thermal variability. *J. Clim.* **33**, 7233–7253 (2020).
48. N. S. Pyko *et al.*, Assessment of cooperativity in complex systems with non-periodical dynamics: Comparison of five mutual information metrics. *Phys. A Stat. Mech. Appl.* **503**, 1054–1072 (2018).
49. G. Di Capua *et al.*, Dominant patterns of interaction between the tropics and mid-latitudes in boreal summer: Causal relationships and the role of timescales. *Weather Clim. Dyn.* **1**, 519–539 (2020).
50. J. Meng *et al.*, Complexity-based approach for El Niño magnitude forecasting before the spring predictability barrier. *Proc. Natl. Acad. Sci. U.S.A.* **117**, 177–183 (2020).
51. R. W. Reynolds, N. A. Rayner, T. M. Smith, D. C. Stokes, W. Wang, An improved in situ and satellite SST analysis for climate. *J. Clim.* **15**, 1609–1625 (2002).
52. R. W. Reynolds *et al.*, Daily high-resolution-blended analyses for sea surface temperature. *J. Clim.* **20**, 5473–5496 (2007).
53. S. A. Klein, B. J. Soden, N. C. Lau, Remote sea surface temperature variations during ENSO: Evidence for a tropical atmospheric bridge. *J. Clim.* **12**, 917–932 (1999).
54. H. Hersbach *et al.*, The ERA5 global reanalysis. *Q. J. R. Meteorol. Soc.* **146**, 1999–2049 (2020).
55. L. Cheng *et al.*, Improved estimates of ocean heat content from 1960 to 2015. *Sci. Adv.* **3**, e1601545 (2017).

EARTH, ATMOSPHERIC, AND PLANETARY SCIENCES